Journal of Materials Research and Technology 36 (2025) 5366–5380

Contents lists available at ScienceDirect

Journal of Materials Research and Technology

journal homepage: www.elsevier.com/locate/jmrt

Tin fog effect analysis during fluxless soldering under reflow with formic acid: Methodology, mechanism, and reliability impact

Liangzheng Ji [a,b], Xinyue Wang [a], Wenting Liu [a], Xin Wang [b], Wenwu Guo [b], Guoqi Zhang [c], Jing Zhang [b,*], Pan Liu [a,**]

[a] Academy for Engineering and Technology, Fudan University, Shanghai, 200433, China
[b] Heraeus Materials Technology Shanghai Ltd., Shanghai, 201100, China
[c] Electronic Components, Technology, and Materials, Delft University of Technology, Delft, 2628CD, Netherlands

ARTICLE INFO

Handling editor: M Meyers

Keywords:
Fluxless solder paste
Formic acid
Tin fog
Reliability
Mechanism
Mitigation

ABSTRACT

Fluxless tin soldering eliminates flux residues but introduces tin fog, which affects the reliability of electronic packaging. The influence of tin fog was first analyzed through the shear strength of the Al wires bonded on DBC substrates. After aging at 300 °C for 4 h, shear strength increased by 4.5 % on pure copper surfaces but decreased by 22.6 % on tin fog-covered surfaces. Further SEM revealed tin fog created interfacial porosity, reducing strength. Secondly, the impact of tin fog formation during the formic acid reflow process was studied under different formic acid concentrations and different vacuum frequencies during the reflow's preheating stage. Through SEM, EDS, Micro-IR, and XPS tests, the principal components of tin fog were identified as elemental tin, tin dioxide, and organic compounds such as amides and esters. It is found that tin fog forms through a process wherein tin formate produced during formic acid reflow adheres to the substrate surface, which is already adsorbed with organic substances such as esters and amides, and subsequently decomposes at high temperatures to generate derivative products creating the fog. Therefore, to mitigate tin fog formation, tin fog was effectively controlled under a tripled vacuum frequency, resulting in reduced organic residues on substrates. Under such a mitigation strategy, further reliability tests showed that the shear strength of Al wire bonding after aging at 300 °C was comparable to that on clean DBC substrates. This research provides a valuable reference for enhancing the reliability of fluxless soldering in electronic packaging.

1. Introduction

Soldering, an age-old practice with roots in metallurgy, has transformed to become the backbone of modern electronic assembly and interconnection technologies. As the essence of soldering, it entails the joining of the metallic interfaces through the application of a fusible alloy, which typically comprises a mixture of feature elements, such as tin, silver, copper, or alternative lead-free compositions in response to environmental regulations such as RoHS (Restriction of Hazardous Substances) [1,2]. In contemporary electronics manufacturing, the prevailing impetus toward miniaturization, higher performance, and complexity has propelled the engineering of solder materials to achieve reliable intermetallic connections at microscopic scales [2–7].

Solder materials are usually applied to improve the quality of interconnects with the support of fluxes to improve the quality of interconnects. Fluxes facilitate the soldering process by removing surface oxides from the metal, enabling the formation of a clean, oxide-free interface for solder wetting, ensuring adequate wetting between solder and substrates, and preventing new oxides from forming during the soldering process [3,8]. However, fluxes present inherent challenges, particularly due to the residues they leave behind. These residues pose significant post-soldering reliability concerns, such as corrosion under humid conditions, reduction in surface insulation resistance, increased leakage current, and the potential for electrochemical migration and dendrite formation on PCBAs (Printed Circuit Board Assemblies) [9,10]. In response to such challenges, fluxless soldering emerges, often utilizing advanced technologies such as plasma, laser, or ultrasonic-assisted soldering to facilitate oxide removal and surface activation, which holds promise in mitigating the limitations associated with flux-dependent processes through fundamental reconfigurations [11,

* Corresponding author.
** Corresponding author. Academy for Engineering & Technology, Fudan University, Shanghai, 200433, China.
E-mail address: panliu@fudan.edu.cn (P. Liu).

https://doi.org/10.1016/j.jmrt.2025.04.151
Received 5 March 2025; Received in revised form 9 April 2025; Accepted 14 April 2025
Available online 15 April 2025

12]. One popular fluxless approach in soldering is the utilization of formic acid to produce a reductive atmosphere, which enhances solderability. Investigations have encompassed soldering under formic acid regarding wettability, contact angle behavior, and thermogravimetric analysis [13–18].

Among the challenges of formic acid fluxless soldering, surface contamination, especially with tin, was noticed as a challenge. Tin fog, colloquially referred to as a "grey circle," refers to residual tin-containing material that could result from the decomposition of tin formate formed during the reaction between formic acid and tin-based alloys [13,14,19]. Conti and Mokhtari have turned their attention to the deposits surrounding solder joints in fluxless soldering applications using formic acid, referring to these deposits as "crystal". They utilized a variety of analytical techniques, including Scanning Electron Microscopy (SEM), Energy Dispersive Spectroscopy (EDS), X-ray Diffraction (XRD), Fourier Transform Infrared Spectroscopy (FT-IR), and Thermogravimetric Analysis (TGA), to conduct a comprehensive assessment of the material's properties [15,16,20]. Through these investigations, they probed the reaction behavior between tin and its oxides with formic acid and the reaction products' subsequent evaporation and degradation behaviors. Nisikawa and He defined the phenomenon as "tin steaming", which likely occurs when gaseous tin formate deposits and decomposes during reflow, similar to Conti and Mokhtari's opinions. They also observed that the chemical reaction leading to tin fog is accelerated by higher peak temperatures and prolonged heating times during formic acid soldering [13,14,19]. The presence of such residual material can pose significant risks in terms of short circuits between component terminals, compromising wire bonding strength, and even long-term reliability within power electronic packaging.

To date, there remains a lack of comprehensive investigation into the effects and formation mechanism of tin fog. Therefore, in this study, the impact of tin fog on Al wire bonding reliability on Direct Bonded Copper (DBC) surfaces was specifically investigated, emphasizing the practical application perspective. The formation mechanisms of tin fog during the soldering process and its subsequent effects on the bonding interface were investigated in this study. Through the employment of advanced characterization techniques, including SEM, EDS, Micro-Infrared (Micro-IR), and X-ray Photoelectron Spectroscopy (XPS), a formation mechanism was established, demonstrating that tin fog originated from the decomposition of tin formate, thereby extending prior research contributions. Tin formate adheres to substrates already laden with organic compounds such as amides and esters during high-temperature reflow processes. Subsequently, an investigation was conducted to mitigate the phenomenon of tin fog. The primary method involved optimizing the reflow profile, specifically emphasizing the increase of vacuum frequency during the preheating phase. Furthermore, the influence of formic acid concentration on tin fog generation was evaluated under the optimized reflow conditions. Finally, the effectiveness of these adjustments in mitigating the tin fog phenomenon was evaluated through Al wire bonding and reliability tests under controlled conditions.

2. Experiments and characterization methodology

2.1. Soldered samples preparation

In this study, a formic acid-assisted vacuum reflow process was utilized to prepare the soldered samples for surface contamination analysis. As shown in Fig. 1, fluxless solder paste (which comprises SAC305 Type 3 powder, organic binders, and solvents) was firstly stencil printed onto the DBC substrate, followed by dummy dies (5 mm * 5 mm * 0.2 mm, backside coated by Ag/Ni with a thickness of over 1 μm) picked and placed over the deposited paste. Such sandwich structure underwent the reflow process, as detailed in the schematic diagram shown in Fig. 2 using a Pink Vadu200 oven. The detailed reflow condition contains the typical programmed heating steps. Throughout the heating process, the following operations were performed: vacuum extraction, nitrogen gas introduction, and formic acid introduction within specific temperature ranges.

2.2. Wire bond and shear strength test

To investigate the surface cleanliness of the soldered samples on the DBC substrate, a series of wire bonding experiments were conducted to study the shear strength between the bonded wire and the substrate. Al wires with a thickness of approximately 380 μm from Heraeus were bonded to the soldered substrates. The bonding equipment used was from Kulicke & Soffa (model: ASTERION). Subsequently, the bonded samples underwent shear testing to compare the strength between the fluxless solder sample and the bare substrate. The testing was conducted using equipment from Nordson DAGE, referring to the JEDEC standard wire bond shear test method JESD22-B116A. Each sample was bonded with 16 Al wires, resulting in a total of 32 bonding points. The shear height was 20 μm, and the shear speed was 300 μm/s.

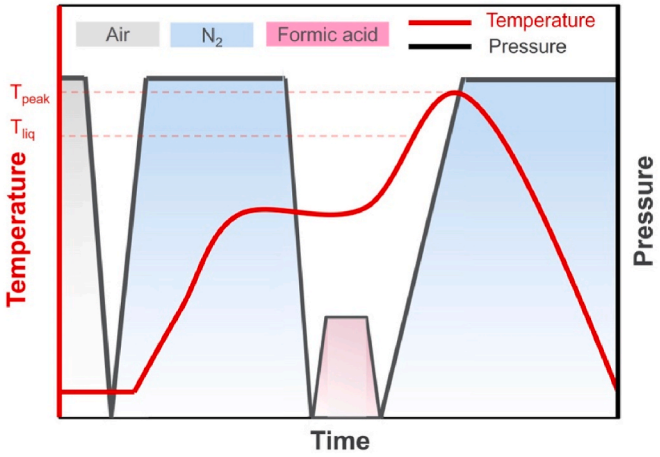

Fig. 2. Schematic diagram of the formic acid-assisted vacuum reflow process involving the temperature and conditions.

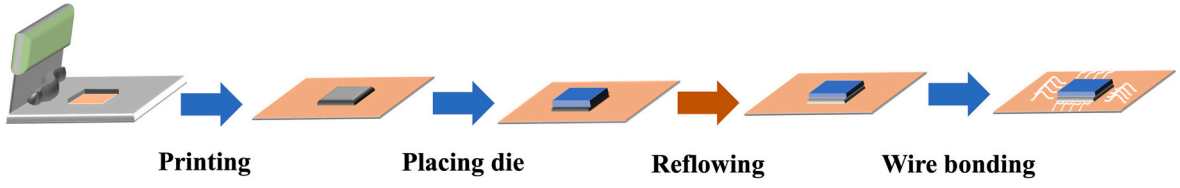

Fig. 1. Schematic diagram of the application process flow for the sandwich sample preparation.

2.3. Characterization methodology

The occurrence of tin fog was primarily detected using a digital camera, followed by Scanning Electron Microscopy with Energy Dispersive X-ray Spectroscopy (SEM/EDS) from Phenon, as well as the fracture surface and the cross-sections of wire-bonded samples. The KEYENCE VHX-7000 microscope was applied to take high-resolution optical images of the fracture surface. The Microscopic infrared spectroscopy (Micro-IR) (PerkinElmer, Spotlight 4000) was used to observe the surface contamination and analyze organic residuals on the surface; Scanning Electron Microscopy with Energy Dispersive X-ray Spectroscopy (SEM/EDS) from Phenon was employed to observe the surface and analyze the distribution of elements on the surface; the surface organic residuals and tin fog of the soldered samples were characterized using X-ray Photoelectron Spectroscopy (XPS, Shimadzu, AXIS SUPRA+). For XPS analysis, Al Ka radiation (l486.6 eV) was utilized to study the chemical structure of tin (Sn), copper (Cu), carbon (C), oxygen (O), and nitrogen (N) on the contaminated surface of the soldered samples.

3. Results and discussion

3.1. Tin fog phenomenon and SEM/EDS characterization

In this study, fluxless solder paste was utilized in conjunction with a designated reflow profile to facilitate the soldering of dummy chips onto DBC substrates, resulting in a structured assembly depicted optically in Fig. 3. Notably, this figure illustrated a substantial coverage of a grey material on the DBC surface, identified as tin fog, which was distributed irregularly across the substrate.

To further characterize the post-soldering surface, SEM was applied, providing a detailed analysis at multiple selected positions progressively distanced from the chip edge: 3 mm for Area A, 6 mm for Area B, and 9 mm for Area C, with Area C aligning nearly at the interface of the contaminated (tin fog) and clean areas visually. Fig. 3 illustrates this with (a) providing the schematic diagram, and (b) displaying the optical image. Fig. 4 showcases SEM images from Areas A, B, and C of the sample's DBC surface under various magnifications, where substantial tin fog phenomena could be observed.

At Area A, as displayed in Fig. 4 (a), the DBC surface texture and distinct grain boundaries were visible, free of large tin particles, while black dots marked copper grain junctions. Increments in magnification revealed different structures; for instance, Fig. 4 (b) exhibited pronounced spindle-shaped structures indicative of tin-containing particles. Fig. 4 (c) displayed an almost complete layer of tin enveloping the substrate surface. Transitioning to Area B, droplet-like tin particles were observed in Fig. 4 (d) and 4 (f), with block-like tin particles covering the surface visible in Fig. 4 (f). Across these observations, the structures predominantly existed at the nanoscale. Upon examining Area C, as depicted in Fig. 4 (g) and 4 (h), similar droplet-like tin particles were present at even smaller scales, with an overall reduced distribution density. Notably, in Fig. 4 (c) within Area C, much smaller tin particles were visible as bright white spots, indicating the presence of tin fog at the nanoscopic level.

Furthermore, Fig. 4 (c) representing Area A, Fig. 4 (d) representing Area B, and Fig. 4 (h) representing Area C, were chosen for quantitative analysis using Image J software, relating them to Fig. 5(a) and 5 (b), and Fig. 5 (c) respectively. As depicted in Fig. 5 (d), the average particle size and the area ratio of tin fog are presented. Specifically, the average particle size in Area A is 2562.48 nm^2 with an area ratio of 21.11 %. In Area B, the values decreased to 1183.20 nm^2 for the average particle size and 12.18 % for the area ratio. Moving further to Area C, the average size is 431.19 nm^2, and the area ratio is 6.86 %. These measurements indicate that the particle size of the tin fog is on the nanometer scale.

The progression from farther areas to closer inspection showed an increase in both the density and size of tin particles, consistent with nucleation and island growth theories in surface chemistry. This gradual increase and the transition from macroscopic observations of tin fog to microscopic validation of nanoscale tin particles describe the underlying dynamics of the tin fog formation.

Following preliminary analyses, a targeted region in Area A was selected for EDS mapping, with the corresponding results presented in Fig. 6. Fig. 6 (a) displays the SEM image of the corresponding area, while Fig. 6 (b) and (c) respectively show the distributions of Cu and Sn. Fig. 6 (d) through (f) depict the distribution of C, N, and O within the same area. The elemental distribution by weight percentage is presented in Table 1.

The analysis reveals that copper is the predominant element on the surface, constituting 93.5 % of the weight percentage, indicating that the surface is largely characterized by the copper substrate. Tin is scattered across the surface, comprising 3.1 % of the total elemental composition, suggesting sporadic distribution rather than uniform coverage. Intriguingly, significant levels of carbon, nitrogen, and oxygen were also detected, each dispersed across the surface in a similar scattered fashion, with carbon at 1.1 %, nitrogen at 2.0 %, and oxygen at 0.3 %.

Despite the apparent severity of tin fog in optical photographs, it actually constitutes a relatively small fraction of the surface composition. The presence and distribution of C, N, and O elements suggest that the tin fog phenomenon may occur in conjunction with organic materials. This observation leads to a preliminary conclusion that tin fog, while visually prominent, is intimately associated with the presence of organic compounds, which could play a significant role in its formation and distribution on the surface. Thus, this analysis not only helps in understanding the elemental makeup of the affected areas but also hints at the underlying chemical interactions that contribute to the manifestation of tin fog in fluxless soldering processes.

3.2. Tin fog effect on the wire bonding and analysis

An experiment was designed to evaluate the impact of tin fog presence on the wire bonding strength on DBC substrates, with an extension to understand the effects of thermal aging. The specimens underwent a

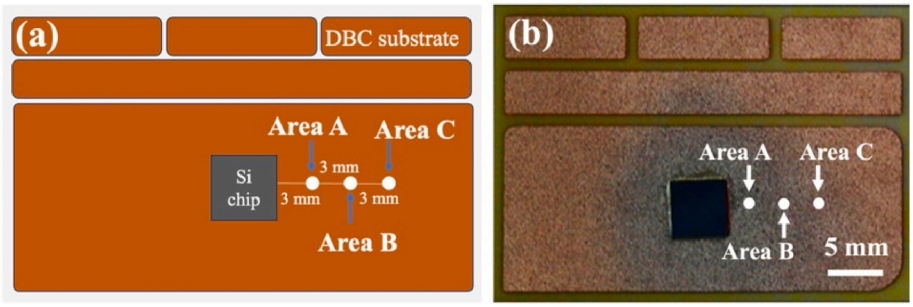

Fig. 3. (a) Schematic diagram of the selected position, (b) optical image of the soldered sample covered with tin fog.

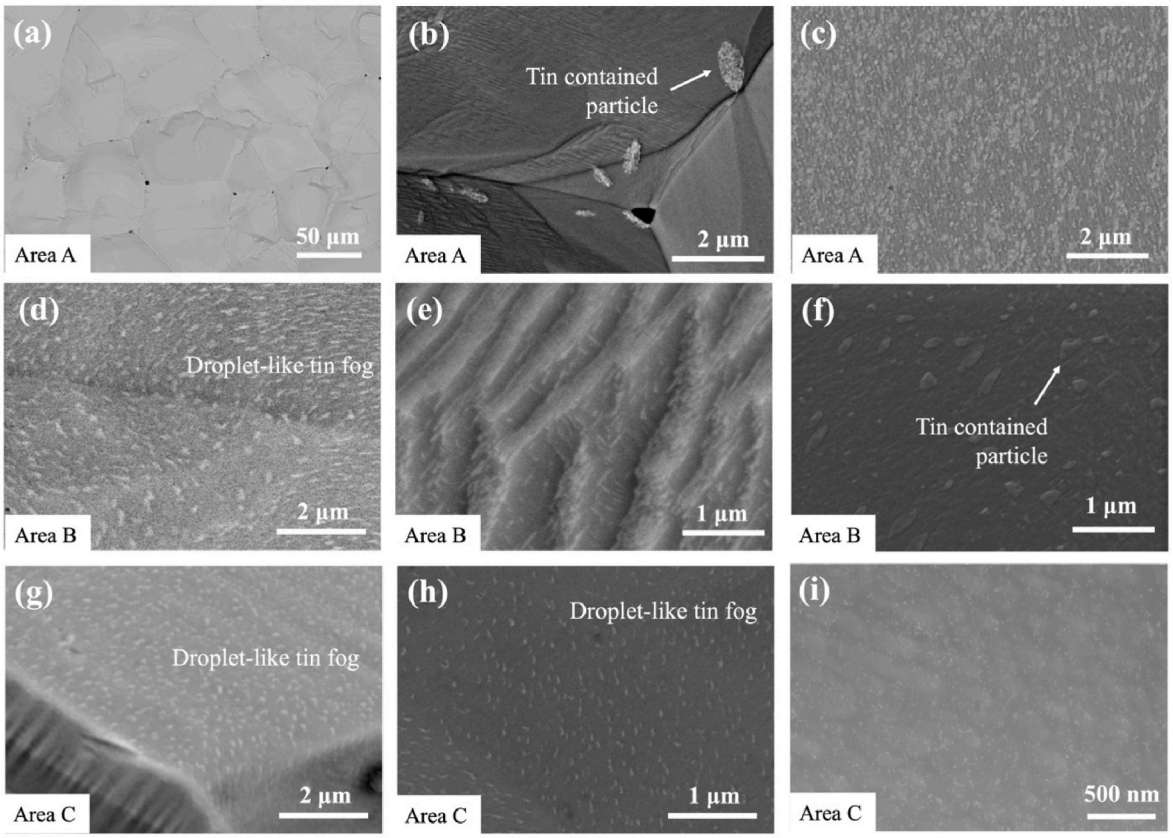

Fig. 4. SEM images at various magnifications of the DBC surface through the reflow profile a: (a), (b), and (c) the area A; (d), (e), and (f) the area B; and (g), (h), and (i) the area C.

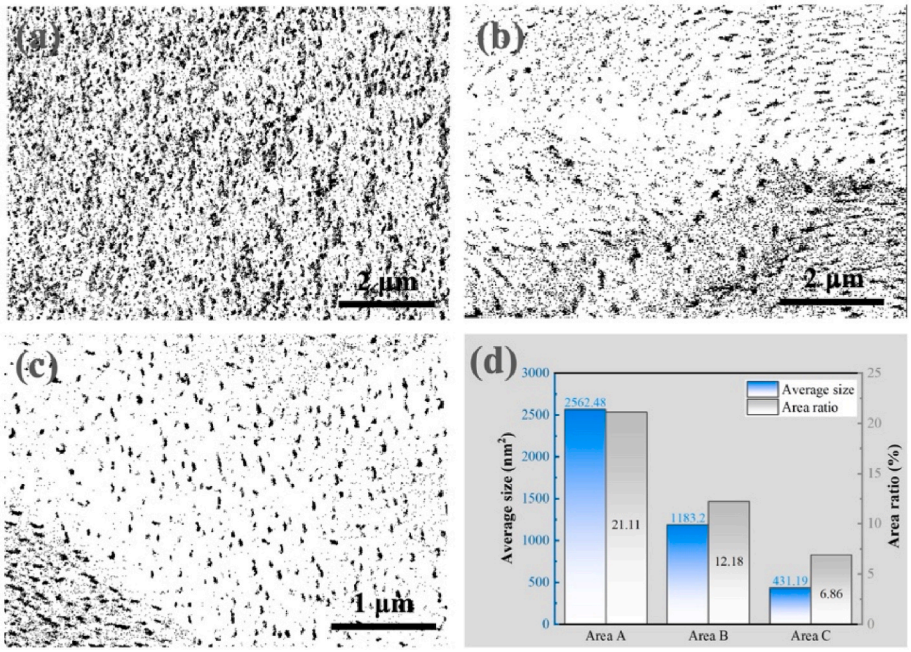

Fig. 5. Image J output images from (a) Fig. 4(c)–(b) Fig. 4 (d), and (c) Fig. 4 (h). (d) Average size and area ratios for each respective area.

thermal aging process in a muffle furnace at 300 °C for 4 h, a condition determined based on prior research from our team aimed at simulating moderate high-temperature stress typical in wire-bonding applications.

As shown in Fig. 7, the initial average shear strength of Al wire bonds on clean DBC substrates was measured at 2103.3 g, with a standard deviation of 161.9 g. Notably, following the thermal aging process, an increase in shear strength was recorded, with an average post-aging value of 2198.9 g and a standard deviation of 220.9 g. This 4.5 %

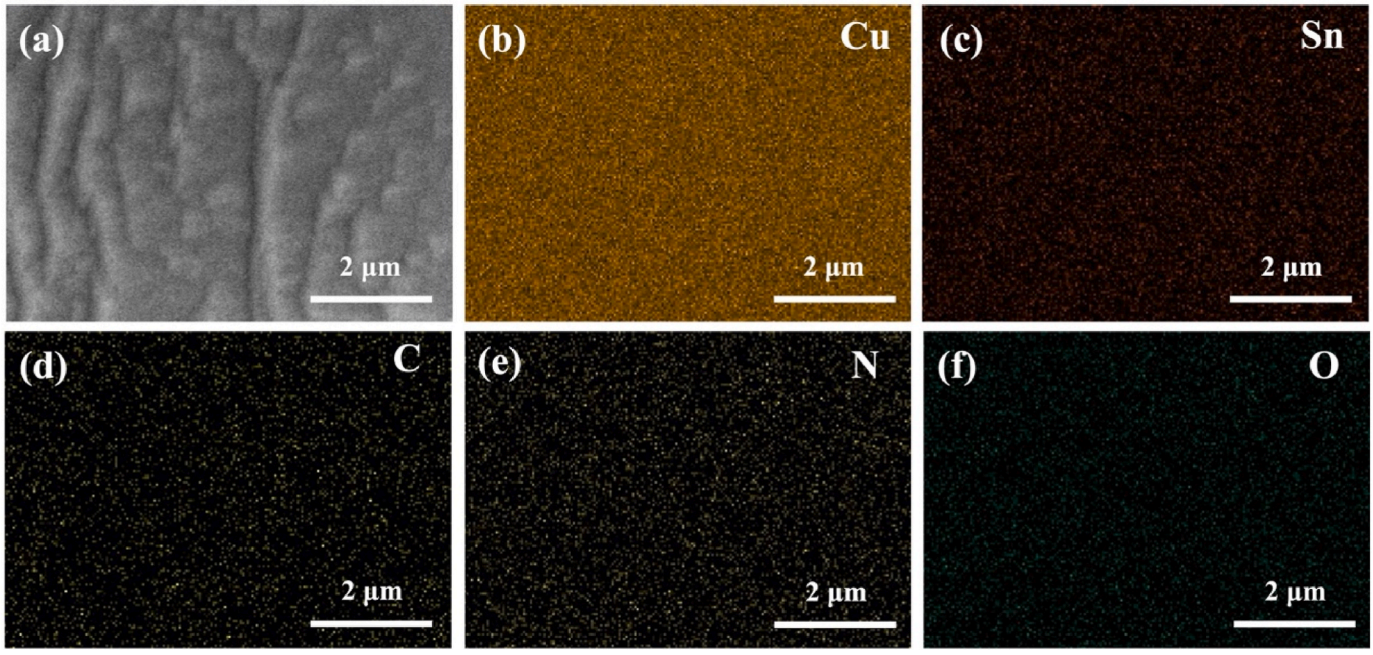

Fig. 6. (a) The SEM image of specific area location within Area A, the EDS mapping results of the corresponding area of element (b) Cu, (c) Sn, (d) C, (e) N, (f) O.

Table 1
EDS results of elemental compositions.

Elements	Wt (%)
Cu	93.5 %
Sn	3.1 %
C	1.1 %
N	2.0 %
O	0.3 %

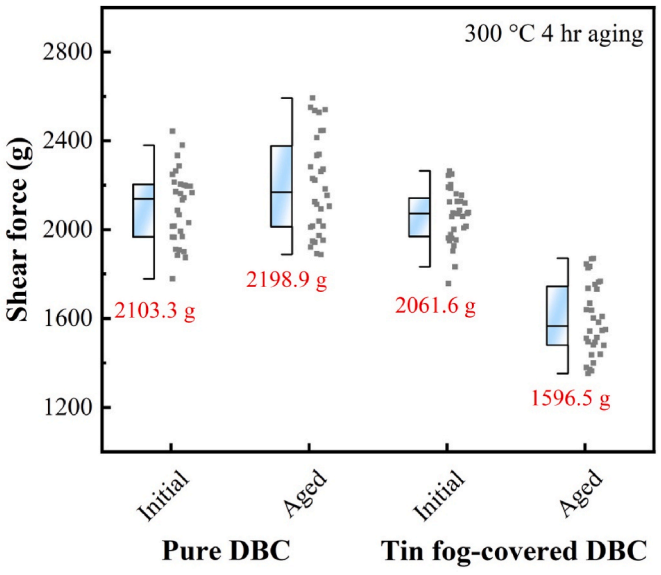

Fig. 7. The shear strength comparison between bare Cu and tin fog area before and post-aging.

increment in shear strength could potentially be attributed to enhanced intermetallic compound (IMC) formation at elevated temperatures, which might have contributed to a more mechanically robust bond interface, thereby improving the overall structural integrity of the bond.

In contrast, DBC substrates with the presence of tin fog exhibited an initial bond strength of around 2061.9 g, marginally lower than that of their clean counterparts, with a standard deviation of 120.2 g. This suggests an initial detrimental effect of tin fog on the bonding interface, potentially due to the presence of non-conductive oxides or mechanical interference during the wire bonding process. Significantly, post-aging measurements demonstrated a drastic reduction in strength to 1596.5 g, with a standard deviation of 162.7 g. This substantial 22.6 % decrease in strength by 465.1 g might indicate exacerbated degradation mechanisms, such as the deterioration of bond integrity or the acceleration of IMC layer growth in an inhomogeneous manner, which could compromise the bond's mechanical stability.

From the OM and SEM images of the fracture, as shown in Fig. 8 and (a) shows the interface on a pure DBC surface with an Al wire before aging, where residual aluminum indicates a strong initial bond. Similarly, Fig. 8 (b) displays the interface on a tin fog-covered DBC surface with bonded Al wire before aging, also with visible residual Al, suggesting a good bond. Post-aging, Fig. 8 (c) shows the interface on a pure DBC surface where the residual Al covers the bond area extensively, signifying an increase in strength. However, Fig. 8 (d) reveals the post-aging interface on a tin fog-covered DBC surface with no significant residual Al, implying a weaker bond. Fig. 8 (e) shows a section of pure DBC surface post-aging, where a predominantly ductile fracture indicates maintained structural integrity. Conversely, Fig. 8(f–h) displays the tin fog-infected surfaces, revealing porous, honeycomb-like structures at various magnifications reflected in the significantly reduced shear strength. The presence of oxidized tin, participating in the diffusion process, exacerbates the formation of structural inhomogeneities, and severely influences the bond's mechanical reliability.

Subsequently, the role of tin fog on the integrity of wire bonds on DBC substrates has been evaluated, particularly under conditions of thermal stress. Cross-sectional analysis of four distinct sample groups (Fig. 9 a–d) was conducted to visualize the microstructural changes before and after thermal aging at 300 °C for 4 h. In Fig. 9 (a) and (c), the baseline cross-sections of pure DBC surfaces and DBC surfaces with tin fog are depicted, showing the upper aluminum and lower copper layers with no significant initial IMC formation. Notably, even in the presence of tin fog, no distinctive tin-related layers were detected at the Al–Cu interface initially, suggesting that the presence of tin fog does not

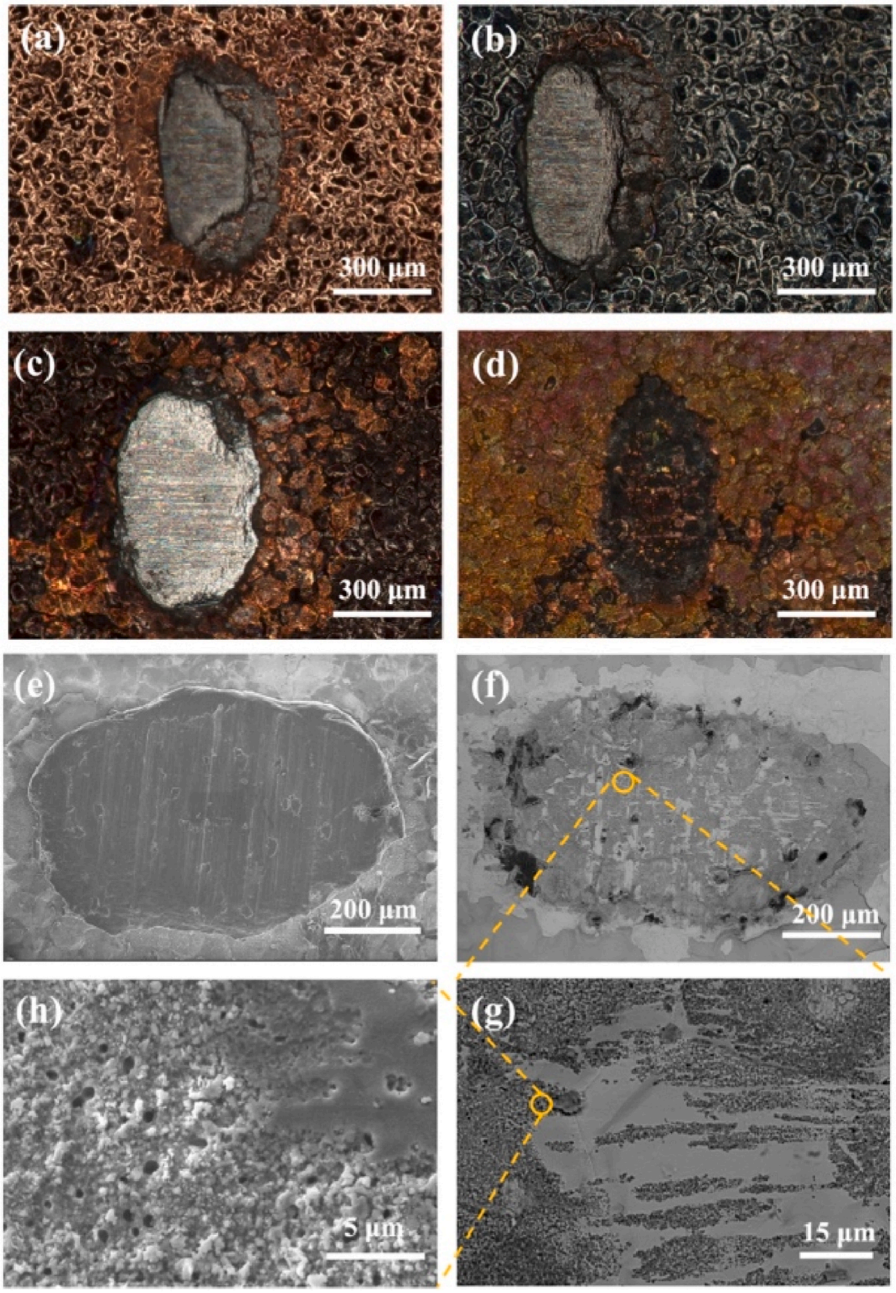

Fig. 8. OM of Cu–Al bonding interface: (a) the initial state of the sample prepared with a pure DBC substrate, (b) the initial state of the sample prepared with a tin fog-covered DBC substrate, (c) the aged state of the sample prepared with a pure DBC substrate, (d) the aged state of the sample prepared with a tin fog-covered DBC substrate. SEM fracture surface of post-aging Cu–Al bonding interface for (e) pure DBC substrate, and (f–g) DBC substrate with tin fog, shown at different magnifications.

directly disrupt the initial metallurgical bonding between these layers.

Contrasting outcomes were evident post-aging, as illustrated in Fig. 9 (b) and (d). For the pure DBC (Fig. 9 b), pronounced diffusion between copper and aluminum was observed. This diffusion led to the formation of a series of IMCs, substantiating the enhanced shear strength observed on pure DBC surfaces post-aging - a direct result of strengthened interfacial bonding due to intermetallic growth. In stark contrast, the tin fog-infected DBC surface (Fig. 9 d) revealed a similar diffusion phenomenon but was accompanied by the development of a continuous porous layer near the copper interface. This layer of porosity, indicative of structural weakness, correlates with the obvious decrease in shear strength. These pores are likely attributable to the disturbance caused by the micro-amounts of tin fog, which, participating in high-temperature diffusion, induce mismatches and void formations in an otherwise homogenous interface.

Additional insights were gained through line scans and atomic distribution mapping in selected areas (Fig. 9 e, f, g, h). The Al–Cu bonding interface on the pure DBC surface bonded with Al wire before aging, as shown in Fig. 9 (e), displays no discernible IMC layer. However, after aging, a distinct Al–Cu IMC layer is formed through the process of diffusion. Fig. 9 (f) illustrates that this layer comprises a series of copper-aluminum intermetallic compounds. Per the literature, these compounds are identified as $CuAl_2$ (tetragonal), CuAl (monoclinic), and Cu_9Al_4 (cubic). The formation of these IMCs directly contributes to an enhancement in strength, a finding that is consistent with the trends reported in literatures [21,22]. For the tin fog-covered DBC surface

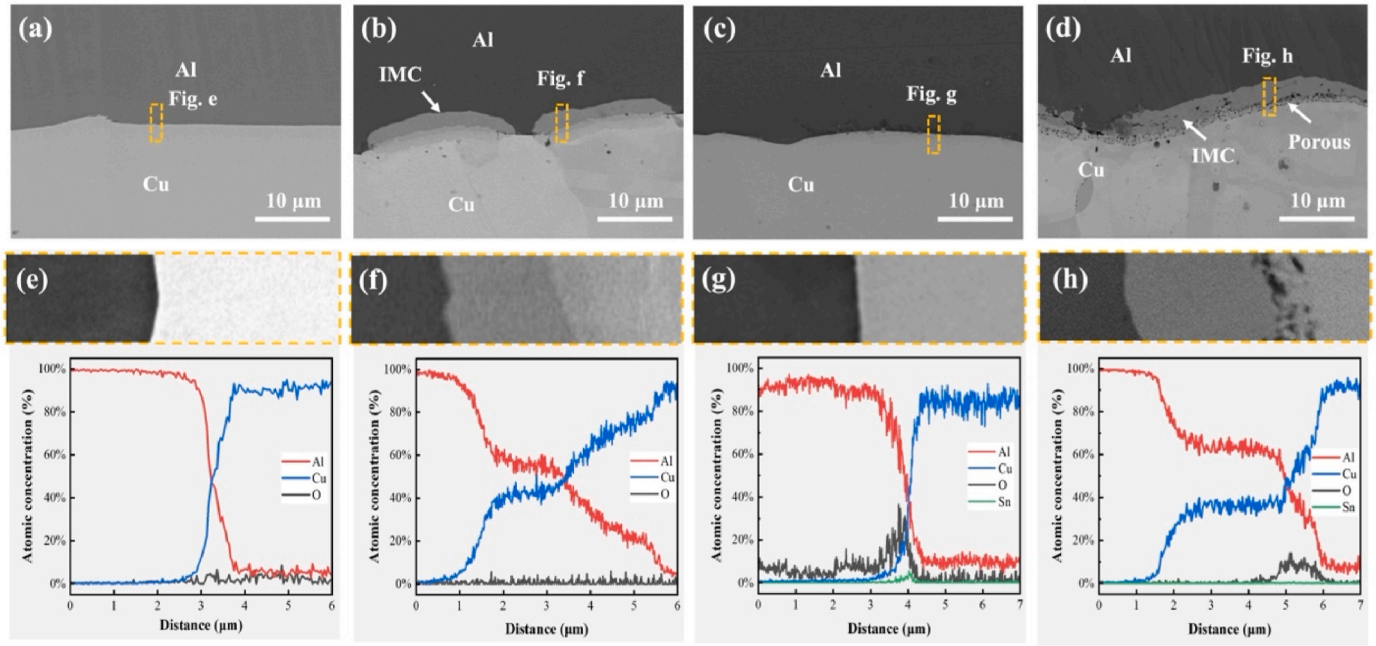

Fig. 9. SEM cross-sectional images of Cu–Al bonding interface: (a) the initial state of the sample prepared with a pure DBC substrate, (b) the aged state of the sample prepared with a pure DBC substrate, (c) the initial state of the sample prepared with a tin fog-covered DBC substrate, (d) the aged state of the sample prepared with a tin fog-covered DBC substrate. The line-scan results for the selected areas: (e) in Fig. a, (f) in Fig. b, (g) in Fig. c, and (h) in Fig. d.

bonded with Al wire, the pre-aging Al–Cu interface shows a significant presence of oxygen and tin elements at the interface, depicted in Fig. 9 (g). Post-aging, as illustrated in Fig. 9 (h), a pronounced IMC layer emerges, and the peak intensity of tin diminishes considerably, suggesting diffusion activities during aging. The reduction in oxygen concentration might be attributed to the formation of a porous structure at the interface during high-temperature diffusion, allowing organic compounds associated with the tin fog to evaporate through these porous channels.

3.3. Tin fog formation mechanism study

3.3.1. The effects of formic acid condition on the tin fog formation

Numerous studies have discussed the formation of tin fog during the fluxless solder paste reflow process with formic acid, emphasizing the strong interaction between tin fog formation and the acidic environment. To deepen our understanding and further investigate the influence of formic acid, an experimental setup was designed, as detailed in Table 2, focusing on the control adjustments during the reflow process.

As illustrated in Fig. 10, three distinct reflow profiles were developed for this purpose. Detailed in Table 2, reflow profile a, employed a formic acid pressure of 100 kPa, maintained for 2 s after reaching the set pressure. In contrast, reflow profile b reduced the formic acid pressure to 50 kPa while maintaining the duration constant. Profile c is built upon the conditions of profile b but substituted formic acid with nitrogen gas.

These reflow conditions were employed to produce three separate soldering samples, each subject to one of the aforementioned reflow profiles. This experimental approach allowed us to systematically examine the effects of different formic acid pressures and the substitution of formic acid with nitrogen on the formation of tin fog.

Three different reflow profiles were applied for soldering, each corresponding to specific atmospheric conditions. The corresponding optical photographs of these samples are displayed in Fig. 11. Fig. 11 (a) relates to the sample processed under reflow profile a, which involved a high formic acid environment at 100 kPa. Fig. 11 (b) corresponds to reflow profile b, which used a reduced formic acid pressure of 50 kPa. Optical examination of these two samples reveals surfaces covered by a grey tin fog. However, the boundaries of this fog are not distinctly identified, particularly in Fig. 11 (a), where the spread of tin fog appears substantially greater. The sample of Fig. 11 (c) was produced under reflow profile c, which substituted formic acid with nitrogen at 50 kPa. The surface of this sample generally appears cleaner and retains the original color of the DBC substrate. Comparing Fig. 11 (c) to Fig. 11(a) and (b), demonstrating the impact of formic acid on the tin fog formation. However, a noticeable ring of residue encircles the chip area, which is preliminarily hypothesized to be organic residues.

Table 2
Reflow parameters under formic acid condition.

Reflow profile	a	b	c[a]
Number of vacuum evacuation	1	1	1
Formic acid pressure (kPa)	100	50	50
Formic acid duration (s)	2	2	2
Peak temperature (°C)	244.4	247.6	245.6
Time above liquid (>217 °C, s)	101	108	105
Preheat time (150–200 °C, s)	389	381	378

[a] Formic acid was replaced by N_2.

3.3.2. EDS characterization on the distribution of tin fog across the substrate

To further quantify the distribution of tin fog on the surface, an EDS analysis on the produced substrates was conducted to measure the tin content across different areas. As depicted in Fig. 12 (a), the results include measurements of tin content at distances of 3 mm, 6 mm, 9 mm, 12 mm, and 15 mm from the chip edge for samples a, b, and c. The specific test locations are illustrated in Fig. 12 (b). Fig. 12 (a) presents the results across the three samples. For sample a, the weight percentage of tin gradually decreases from 3.53 % at 3 mm from the edge to 0.81 % at 15 mm, showing a distinct downward trend. Similarly, for sample b, a comparable decreasing trend was observed, with tin percentages reducing from 1.47 % down to 0.2 %. A comparison across similar distances from the chip edge between samples a and b shows that the tin content in sample b is consistently lower than in sample a. This suggests a correlation between higher formic acid content and more severe tin

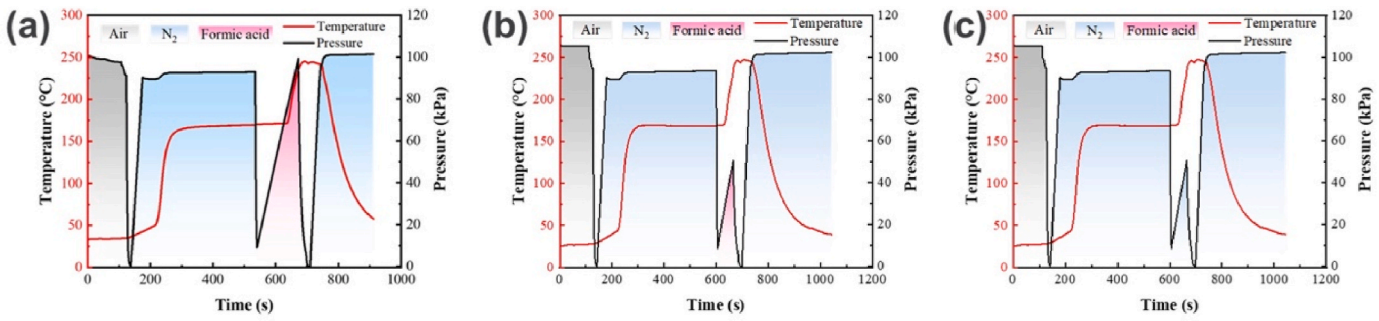

Fig. 10. The diagram of reflow profiles of (a) profile a, (b) profile b, and (c) profile c.

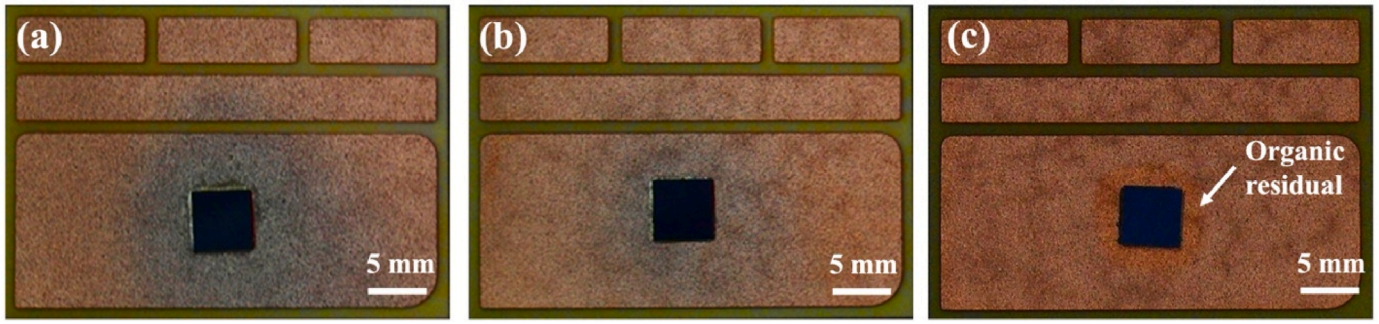

Fig. 11. Optical images of the prepared sample on DBC corresponding to the reflow profile (a) reflow profile a, (b) reflow profile b, and (c) reflow profile c.

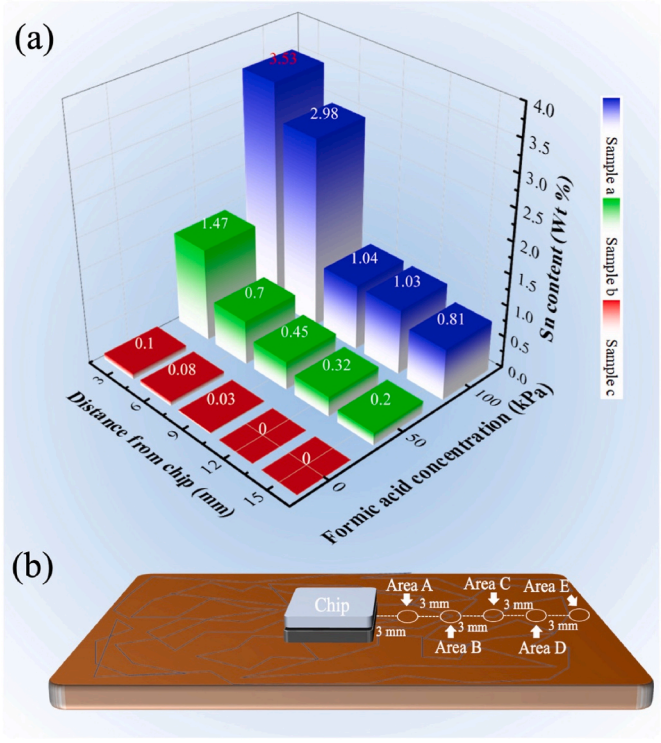

Fig. 12. (a) The tin content distribution in different areas across the DBC substrate for prepared samples a, b, and c, (b) the schematic diagram of the testing positions on the DBC substrate.

fog. Transitioning to sample c, where nitrogen gas replaced formic acid, the results, also shown in Fig. 12 (a) for a formic acid concentration of 0 kPa, demonstrate tin contents of 0.1 %, 0.08 %, 0.03 %, 0 %, and 0 % across the measured points. Notably, no evident tin fog was observed on the surface of this substrate. The profound absence of tin fog in optical photographs under no formic acid conditions and the minimal tin content on the DBC substrate further substantiate that the grey substance present on surfaces in other scenarios is indeed tin fog and is highly associated with the presence of formic acid. These findings elucidate that the tin fog observed on substrate surfaces is directly influenced by the amount of formic acid used in the reflow process, implicating formic acid as a critical factor in the formation and prevalence of tin fog in fluxless soldering environments.

3.3.3. FTIR and Micro-IR characterization on fluxless solder paste and tin fog area

During our investigation of tin fog phenomena using SEM-EDS, significant signals of organic constituents such as C, O, and N were detected, forming a notable portion of the spectral analysis. This initial finding prompted a deeper examination of the surface chemistry using Micro-IR. A detailed comparative analysis was carried out using Micro-IR to study the surface chemical composition across different samples: fluxless solder paste, the organic residual area of sample c, and the area A of samples a, b, and c. Additionally, the contamination around the chip in sample c was characterized, with the results presented in Fig. 13.

Special attention was given to the area surrounding the chip in sample c, where noticeable contamination was observed. The Micro-IR analysis helped identify specific chemical entities contributing to the contamination. IR spectral comparison of the fluxless solder paste with samples a, b, and the targeted region of sample c enabled clear differentiation of chemical environments resulting from varying soldering parameters. Fig. 13 (a) displays comparative IR spectroscopy analyses of the samples. Notably, the signals from areas A of samples a, b, and c are substantially weaker than those from the fluxless solder paste and the organic contaminants in sample c. This denotes a lower degree of organic residues or alterations in the chemical composition in these areas. Fig. 13 (b) shows the baseline IR spectrum of the fluxless solder paste, with peaks identifiable at 1642.8 cm^{-1} for carbonyl groups and at 2872.17 cm^{-1} and 2925.4 cm^{-1} for C–H vibrations [23]. A broad peak at 3349.1 cm^{-1}, attributable to typical hydrogen bonding among hydroxyl,

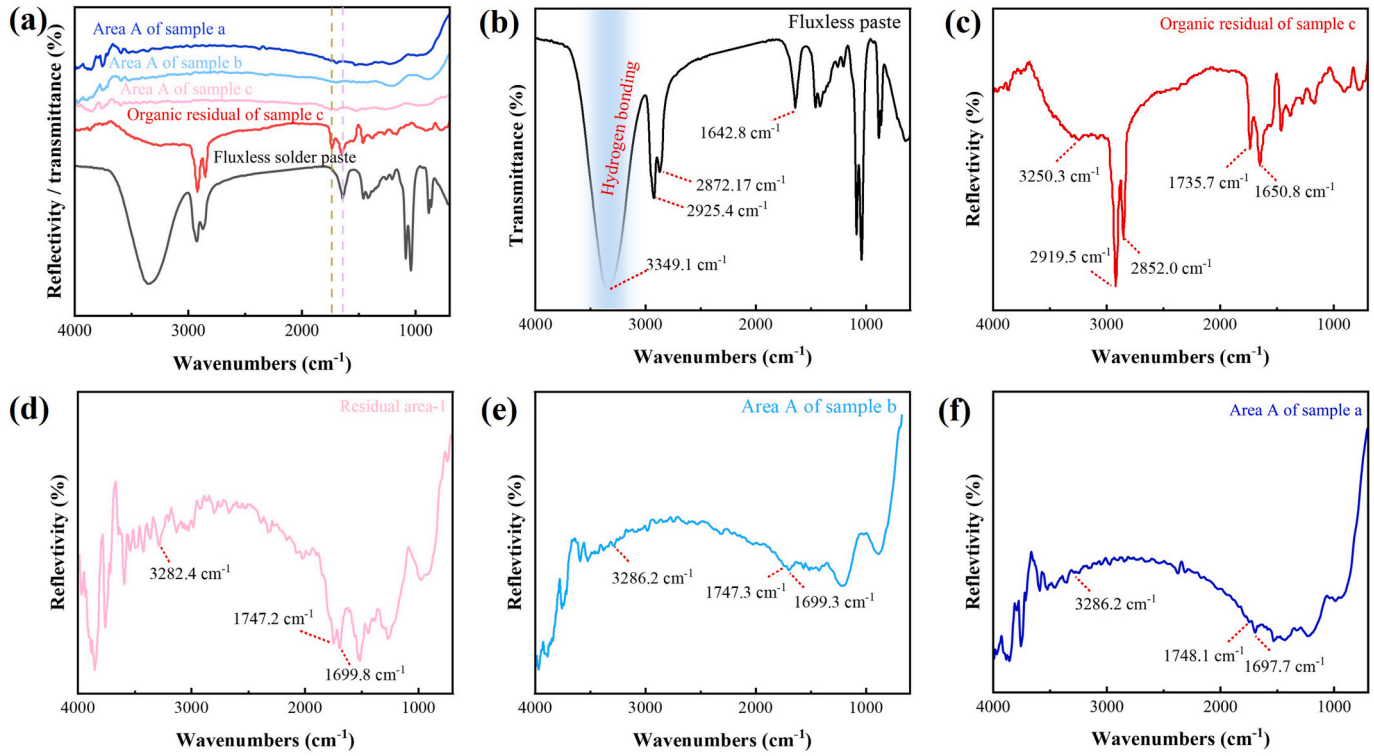

Fig. 13. (a) IR spectrum comparison among the tin fog areas, residual, and fluxless solder paste, (b) the FTIR spectrum of fluxless solder paste, the Micro-IR spectrum of (c) the organic residual area of sample c, (d) the area A of sample c, (e) the area A of sample b, (f) the area A of sample a.

ester, and amide groups, was also observed [24]. Fig. 13 (c) illustrates the IR spectrum of the organic contaminants from sample c, revealing distinct chemical signatures. New peaks at 1650.8 cm^{-1} and 1735.7 cm^{-1} suggest potential ester or amide functionalities [25], while shifts in C–H vibrations to 2852.0 cm^{-1} and 2919.5 cm^{-1}, and the disappearance of the broad hydroxyl peak further indicate chemical transformations on the substrate surface during heating.

Even in regions distanced from visible organic material, as demonstrated in Fig. 13 (d), organic signals persisted, detected at 1747.2 cm^{-1} for carbonyl groups [25], typically from carboxylic acids and amides. A peak at 3282.4 cm^{-1} likely indicated N–H bonds. Similar findings in Fig. 13 (e) and (f) for areas A of samples b and a, respectively, confirmed the presence of organic materials even amidst tin fog, suggesting adsorption onto the DBC surface during reflow.

This comprehensive analysis validates that organic residues are intricately involved in the formation of tin fog, with notable persistence and transformations of organic compounds detected across different sample areas under varying soldering conditions. The organic material identified in the tin fog areas is most likely composed of compounds containing carbonyl-like amide or ester groups.

3.3.4. XPS characterization on tin fog area

In this study, XPS was deployed to conduct high-resolution spectral analyses on areas A of samples a, b, and c, as well as the contaminated region around the chip in sample c, utilizing parameters including C-1s, O-1s, N-1s, Sn-3d, and Cu-2p spectra. The results, presented in Fig. 14, provide a deeper understanding of the surface chemistry variations among these different sample conditions.

Fig. 14 (a) displays the XPS spectrum for the central contaminated area of sample c, revealing detailed spectral information across multiple elemental spectra. The C-1s XPS spectrum highlighted three key peaks: at 284.80 eV for C–C bonds suggesting simple carbon linkages, at 286.57 eV for C–O bonds indicating the presence of oxygen-bonded carbon structures, and at 288.67 eV for C═O bonds, typical of carbonyl functionalities, underscoring a complex organic molecular presence [23,25–27]. Peaks in the O-1s XPS spectrum at 530.78 eV, 531.99 eV, and 533.41 eV are assigned to constituents such as SnO_2, direct C═O linkages, and C–O linkages respectively [26,27], suggesting substantial interactions between tin derivatives and complex organics. The N-1s spectrum displays a peak at 399.72 eV indicative of NH_2 groups, hinting at the presence of amino functional groups which are likely components of the observed residues [27]. The Sn-3d XPS spectrum from Fig. 14 (a) presents a high-resolution analysis at 486.72 eV and 495.14 eV demonstrating the presence of SnO_2 with noticeable signals of elemental tin at 484.51 eV and 492.91 eV [28]. This indicates a major presence of oxidized tin within an organic matrix with polar functional groups. Additionally, the Cu-2p XPS spectrum provides insights into copper presence, with key peaks at 932.47 eV and 952.13 eV, further affirming the integral role of copper [29,30]. This figure corresponds to Area A of sample c, providing insight into the cleaner sections of the substrate distanced from central contamination.

In the C-1s XPS spectrum of Fig. 14 (b), peaks are observed at 284.69 eV for C–C bonds, 286.34 eV for C–O bonds, and 288.41 eV for C═O bonds, indicating the presence of carbon-based compounds, albeit at reduced intensities compared to the more contaminated central area. The O-1s spectrum in Fig. 14 (b) displays a peak at 530.46 eV, suggesting the presence of metal oxides, and peaks at 531.33 eV and 532.58 eV for carbonyl and ether functionalities, respectively. The presence of N-1s at 399.72 eV suggests amine groups. The Sn-3d spectrum is notably quieter, signifying a decrease or absence of detectable tin, reflecting a cleaner area. However, Cu-2p spectra in Fig. 14 (b) reveal copper signals at 932.36 eV and 952.04 eV, with additional peaks suggesting copper (I) oxide presence at 934.51 eV and 954.00 eV.

Corresponding to Area A of sample a, Fig. 14 (c) reveals the C-1s peaks at 284.70 eV, 286.38 eV, and 288.50 eV relating to C–C, C–O, and C═O bonds, respectively, indicating ongoing complex organic presence, similar to Sample c but possibly with varying concentration or subtle interaction differences with tin elements. The O-1s spectrum revealed peaks at 530.79 eV, 532.00 eV, and 533.42 eV, likely corresponding to metal oxides and varying organic functionalities similar to earlier

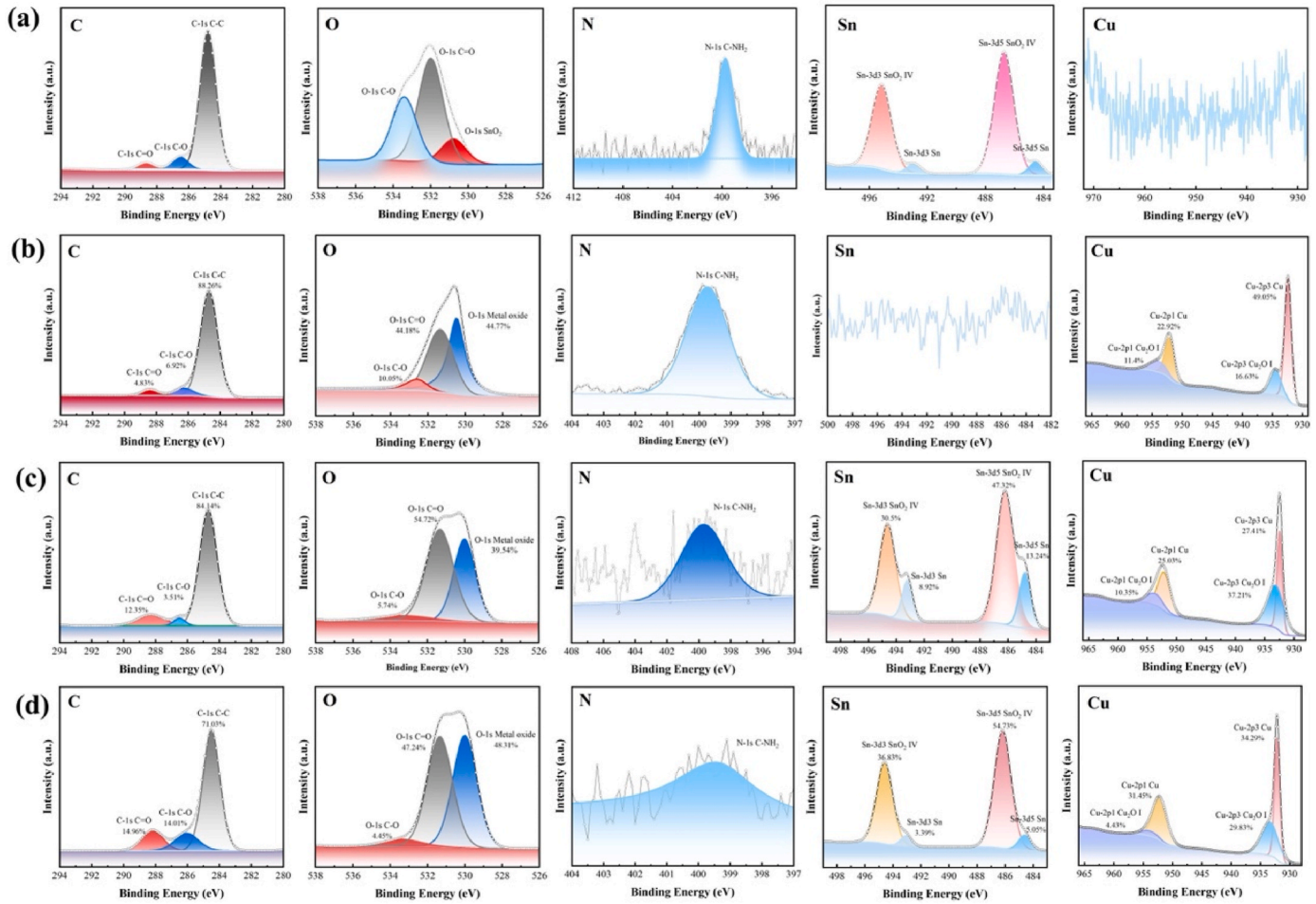

Fig. 14. The XPS spectrum consists of C, N, O, Sn, and Cu of (a) the organic residual area of sample c, (b) the area A of sample c, (c) the area A of sample b, (d) the area A of sample a.

described samples. The Sn-3d spectrum in Fig. 14 (c) shows more activity compared to Fig. 14 (b), with indications of tin presence possibly in oxidized forms, while copper signals in the Cu-2p spectrum are visible at slightly shifted positions compared to previously analyzed samples.

Displaying Area A of sample b, Fig. 14 (d) also provides the C-1s spectrum with peaks at 284.71 eV, 286.39 eV, and 288.51 eV, suggesting similar chemical interactions involving carbon as the other areas, albeit with potentially different environmental impacts or residue levels. The O-1s and N-1s spectra again align with observations indicating complex organo-metallic interactions on the surface, with the Sn-3d and Cu-2p spectra providing further evidence of tin and copper presence, comparable to sample a but in slightly altered concentrations or states due to different reflow conditions.

In conclusion, the XPS data illustrate a clear association between the presence of specific organic compounds and the formation of tin fog. The data reveal that long-chain organics play a crucial role in how tin derivatives deposit and interact on DBC substrates. These findings underscore the complexity of surface chemistry in soldering applications and the potential to control undesirable reactions through precise adjustments in processing parameters.

3.3.5. Proposing the chemical structure of the tin fog area's trace organic residual

EDS analysis revealed distinct C, N, and O signatures in tin fog-affected regions, indicating the presence of characteristic organic constituents. To delve deeper, Micro-IR technology was employed to characterize the minimal organic substances within the tin fog areas. The IR spectra indicated signals of C═O double bonds, typically associated with carbonyl and ester groups. The position of these peaks, albeit consistent with signals from organic contaminants around the chip, exhibited slight shifts due to interactions with the metal surface. These organic components are originally derived from the fluxless solder paste used in the experiments. Further characterization through XPS corroborated these findings, revealing the presence of functional groups such as C═O, C–O, and C–NH_2, alongside signals indicative of long carbon chains. The combination of these analyses suggests that the organic residues primarily consist of long-chain esters and amides. Fig. 15 illustrates the speculated structures of these organic compounds, based on the spectral analysis and observed chemical behaviors. This multifaceted characterization enhances our understanding of the molecular composition associated with tin fog formation, confirming that the significant organic residual components are closely related to the initial materials used in the solder paste. These findings contribute to our grasp of how organic molecules interact within the soldering process, particularly under conditions fostering tin fog formation.

3.3.6. Possible reaction for solder and tin fog formation

During the reflow process of fluxless solder paste in a formic acid environment, several reactions occur, as depicted in the following reactions. These include the oxidation of tin, resulting in either tin oxide (SnO) or tin dioxide (SnO_2), as shown in Equation (1) [28]. In the presence of formic acid during reflow, formic acid can react with tin oxide surrounding the tin particles to form tin formate, especially at elevated temperatures, as depicted in Equations (2)–(4). Similarly, tin

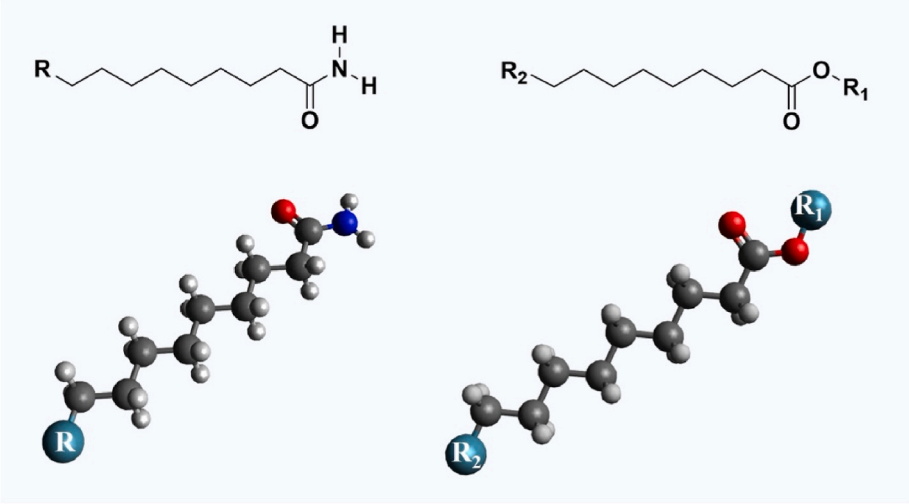

Fig. 15. The proposed chemical structure of the organic compound in the tin fog.

itself can also react directly with formic acid to produce tin formate. According to the literature [15], tin formate decomposes at high temperatures, generating various byproducts such as CO_2, H_2O, and H_2, along with elemental tin and potentially further oxidized forms of tin, as shown in Equation (5). This is also verified by XPS characterization. The XPS analyses of the tin fog surfaces elucidate the chemical states of tin in these residues. The metallic part of the tin fog is primarily composed of tin dioxide, with minor amounts of elemental tin also present. This composition could be attributed either to the direct decomposition of tin formate into tin oxide or to elemental tin produced by the decomposition of tin formate, which then undergoes further oxidation to form tin dioxide [13,15,18,20,31].

$$Sn + O_2 \rightarrow SnO/SnO_2 \quad (1)$$

$$SnO + iHCOOH \rightarrow Sn(HCOO)i + H_2O \quad (2)$$

$$SnO_2 + iHCOOH \rightarrow Sn(HCOO)i + H_2O \quad (3)$$

$$Sn + iHCOOH \rightarrow Sn(HCOO)i + H_2O \quad (4)$$

$$Sn(HCOO)_i \rightarrow Sn + SnO_2 + CO_2 + H_2 + H_2O \quad (5)$$

3.3.7. *Proposed mechanism*

Previous research conducted by other groups has already noted that at certain temperatures, tin powder reacts with formic acid to form gaseous tin formate, which disseminates throughout the atmosphere [13,16]. This tin formate subsequently decomposes, resulting in the deposition of tin and tin oxide on the substrate surface. There is also the potential for more complex chemical reactions to occur that produce tin carbonate, which then decomposes to produce additional tin oxide on the surface [15]. In our experiments, the severity of the observed tin fog phenomenon was directly related to the amount of formic acid present: little to no tin fog occurred in the absence of formic acid. This observation is consistent with previous experimental results from other groups [13,14]. Additionally, we noted that the severity of tin fog is directly correlated with the presence of organic residues on the substrate surface; as the amount of these residues increased, so did the extent of tin fog. One particularly clear observation in our experiments was that the formation of tin fog is invariably associated with the presence of organic substances. SEM, EDS, Micro-IR, and XPS characterizations indicated that these organic substances are likely comprised of long carbon chains with carboxylic and amide groups, and the tin present coexists in either an elemental form or as tetravalent tin. This suggests that tin fog occurs as tin or oxidized states of tin adsorbed onto organic molecules on the metal surface. Therefore, we are more confident that tin fog is a result of the adsorption of polar organic substances on the substrate surface, which then provide active sites for tin adsorption.

Hence, we suggest the following mechanism depicted in Fig. 16. During the reflow heating process, the surface of the tin powder undergoes continuous oxidation, primarily forming tin oxide (SnO) and tin dioxide (SnO_2), as shown in Equation (1). As the temperature increases, the introduction of formic acid gas initiates reactions with tin, tin oxide, and tin dioxide, resulting in the formation of tin formate (depicted in Equations (2)–(4)). This tin formate vaporizes and disperses throughout the entire chamber under high-temperature conditions. Simultaneously, the organic solvents present in the solder paste may experience random flow and volatilization due to the rising temperature. Among these solvents, polar compounds such as amides and esters, owing to their polarity, tend to adsorb onto the surfaces of the surrounding chips. These adsorbed polar solvents create a conducive environment for the tin formate to adhere to the substrate surfaces. Upon further heating during the reflow process, the adsorbed tin formate undergoes thermal decomposition, producing elemental tin. This tin can then undergo additional oxidation to form tin dioxide (SnO_2), as shown in Equation (5), which subsequently adsorbs onto the substrate surface, contributing to the formation of tin fog. Alternatively, the gaseous tin formate dispersed within the chamber may also undergo thermal decomposition and oxidation, leading to the deposition of tin dioxide on the substrate surfaces already laden with polar solvents. This dual pathway highlights the complex interactions and chemical transformations that result in the observable phenomenon of tin fog.

In our future work, we will focus on elucidating the influence of various substrates, beyond Cu-coated ones, on the formation of tin fog, particularly within a formic acid environment. We will investigate the mechanisms by which organic materials adsorb onto different substrate surfaces and subsequently facilitate the adsorption of tin fog.

3.4. *Mitigation measures for the phenomenon of tin fog*

In this research, the crucial role of organic molecules containing carboxyl or amide groups in the formation and surface adsorption of tin fog was investigated. These organic compounds, even in trace amounts, adhere to the metal surface and subsequently bind with tin formate or its decomposition products, thereby contributing to the appearance of tin fog. Notably, formic acid also plays a fundamental role in these interactions.

To delve deeper into the relationship between reflow conditions and the occurrence of tin fog and explore the tin fog mitigation measures,

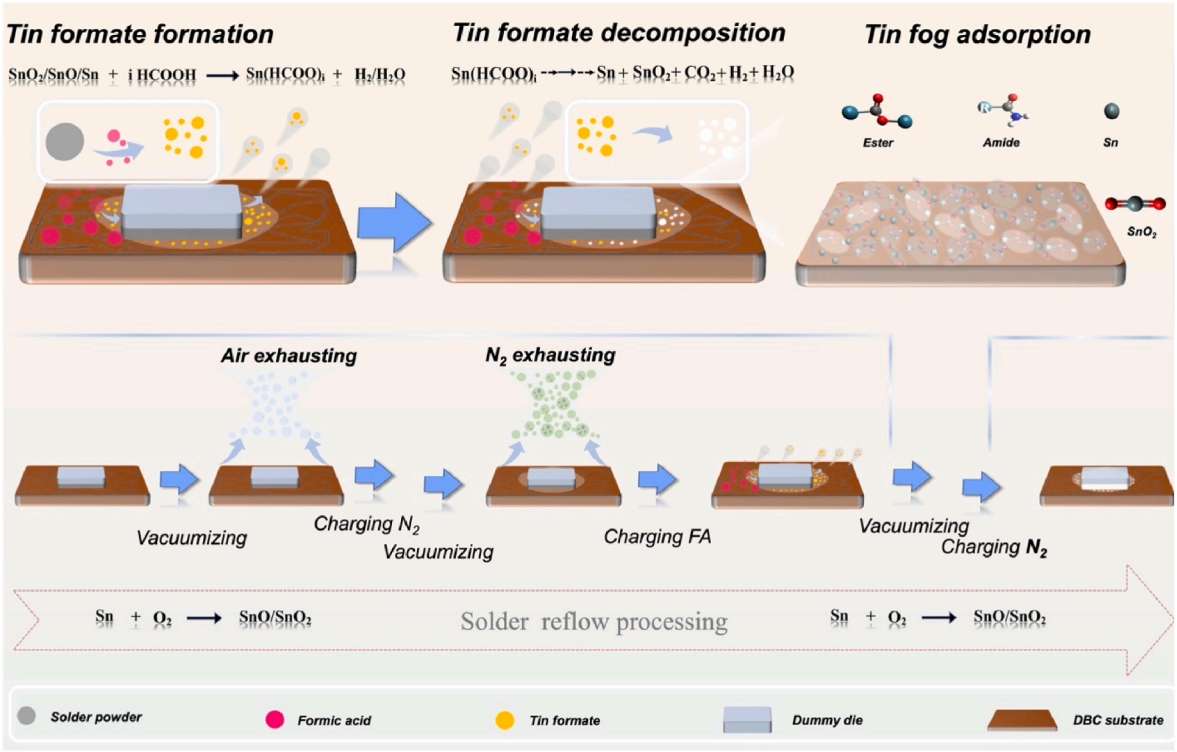

Fig. 16. The proposed mechanism illustrating the in-situ co-occurrence of formic acid and organic residues leading to the formation of tin fog.

four distinct reflow profiles were designed as outlined in Table 3. A key feature of these profiles involved increasing the number of vacuum cycles during the preheat stages to enhance the volatilization of organic substances from the solder paste, thereby reducing their residual presence on the surface. Reflow profile d was developed based on profile c, maintaining the nitrogen atmosphere at 50 kPa pressure for 2 s. Subsequent profiles e, f, and g were modifications based on profile d, where the nitrogen was replaced with formic acid at 50 kPa for 2 s and 100 kPa for 2 s; notably, in profile f, the duration of 100 kPa formic acid exposure was extended to 30 s.

The outcomes of these reflow experiments are depicted in Fig. 17. Fig. 17 (a) shows that compared to Fig. 10 (c), the organic residues surrounding the chip were significantly controlled, with no apparent organic residues observed. This suggests that increasing the vacuum cycles during preheating effectively reduced organic residues on the surface, facilitating the volatilization of organics from the solder paste. Fig. 17 (b), (c), and (d) correspond to the samples processed under profiles e, f, and g, respectively. From an optical perspective, none of these samples exhibited significant grey tin fog deposits on the surface, indicating that the reduction in organic residue adhesion on the substrate surface can substantially control tin fog formation under formic acid reflow conditions, even with increased concentrations of formic acid.

Table 3
Reflow parameters under three vacuum cycles with formic acid for mitigating tin fog.

Reflow profile	d[a]	e	f	g
Number of vacuum evacuation[b]	3	3	3	3
Formic acid pressure (kPa)	50	50	100	100
Formic acid duration (s)	2	2	2	32
Peak temperature (°C)	243.7	246.4	243.3	247.3
Time above liquid (>217 °C, s)	98	101	104	102
Preheat time (150–200 °C, s)	460	466	478	482

[a] Formic acid was replaced by N_2.
[b] Increasing the vacuum twice during the preheating stage, with the vacuum degree approaching zero.

In addition, supplementary experiments were conducted to investigate the impact of different vacuum levels on tin fog formation. Specifically, the vacuum levels of the additional two vacuum cycles were adjusted to 1 kPa and 2 kPa, under the condition of three vacuum cycles, with detailed parameters shown in Table 4. The changes in the surface appearance of tin fog under varying formic acid pressures were examined, with representative results illustrated in Fig. 18. The experimental results indicated that at a vacuum level of 1 kPa and formic acid pressure of 50 kPa, the tin fog was relatively light and controllable (Fig. 18 a). However, when the formic acid pressure increased to 100 kPa, the tin fog became heavier (Fig. 18 b). At a vacuum level of 2 kPa and formic acid pressure of 50 kPa, the tin fog was also heavier and could not be effectively controlled (Fig. 18 c). Consequently, we did not pursue further studies with higher formic acid pressures.

Therefore, this study not only underscores the significance of optimizing the reflow profile to control tin fog but also demonstrates that the tin fog phenomenon can be effectively mitigated through strategic manipulation of soldering conditions, particularly by reducing organic residues.

In our study, as depicted in Fig. 17, no discernible tin fog was observed in the optical photographs of the substrates. Following the methodology outlined in Fig. 12 (b), EDS was conducted to characterize and quantify the tin content across specific areas of these samples. Comparison with sample a was performed, and the results are illustrated in Fig. 19. As shown in Fig. 19 (a), for sample d, under reflow conditions that involved multiple vacuum cycles during the preheat stage and substitution of N_2 for formic acid, the EDS results for tin were similar to those observed in sample c. The weight percentages of tin at distances of 3 mm, 6 mm, 9 mm, 12 mm, and 15 mm from the chip edge on the substrate were respectively 0.17 %, 0.09 %, 0.03 %, 0.07 %, and 0.02 %. These detected elements likely resulted from minor reactions between the activators in the solder paste and the tin powder, with the subsequent diffusion of solvents to the substrate surface, leaving residues of tin-related derivatives after solvent evaporation. For sample e, the respective weight percentages of tin at the same distances were 0.15 %,

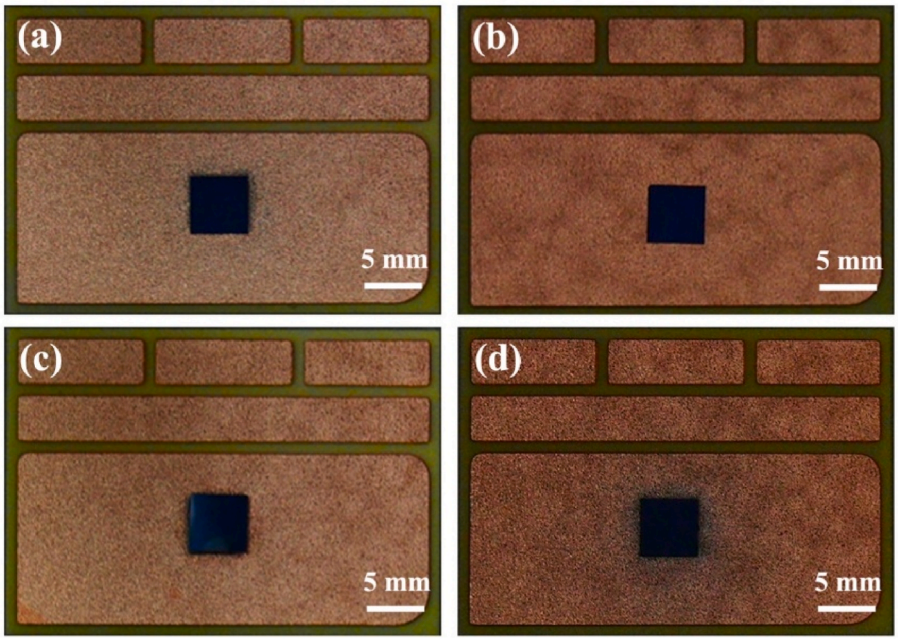

Fig. 17. Optical images of the prepared sample on DBC corresponding to the reflow profile (a) reflow profile d, (b) reflow profile e, (c) reflow profile f, and (d) reflow profile g.

Table 4
Reflow parameters under different vacuum degree with three vacuum cycles tin fog mitigation.

Reflow profile	h	i	j
Number of vacuum evacuations	3	3	3
Vacuum degree (kPa)	1	1	2
Formic acid pressure (kPa)	50	100	50
Formic acid duration (s)	2	2	2
Peak temperature (°C)	245.5	246.7	247.8
Time above liquid (>217 °C, s)	103	105	102
Preheat time (150–200 °C, s)	458	460	461

0.20 %, 0.18 %, 0.16 %, and 0.00 %. In sample f, the percentages were 0.27 %, 0.17 %, 0.22 %, 0.18 %, and 0.2 %, and in sample g, they were measured at 0.26 %, 0.13 %, 0.13 %, 0.05 %, and 0.01 %. When compared to sample a, which exhibited significant tin fog, the optimized samples from d to g demonstrated markedly lower levels of tin presence on the substrate, with concentration levels that were significantly reduced. Despite the increased formic acid concentration from samples d through g, there was no apparent increase in tin levels on the DBC substrates. As shown in Fig. 19 (b), for sample h, the respective weight percentages of tin at the same distances were 0.28 %, 0.21 %, 0.17 %, 0.12 %, and 0.18 %. In sample i, the percentages were 0.80 %, 0.51 %, 0.41 %, 0.30 %, and 0.37 %, and in sample j, they were measured at 0.50 %, 0.43 %, 0.40 %, 0.33 %, and 0.24 %. Compared to the results in Fig. 19 (a), except for sample h where tin fog was well-controlled with less formic acid, the other two conditions showed significantly increased tin fog.

This indicates that with procedural control-specifically using multiple vacuum cycles with high vacuum levels to accelerate the evaporation of solvents and other organic substances-the deposition of tin can be effectively managed. This supports the mechanism that while formic acid plays an important role in tin fog formation, the adsorption of tin formate complexes on residual organics is a crucial factor in the generation of tin fog. This understanding helps in refining process parameters to mitigate tin fog formation effectively, demonstrating the critical role of both formic acid and organic residues in this process. Generally, in the welding process, more formic acid is beneficial for ensuring welding quality as it enhances wettability. Based on our findings, we believe that under the premise of controlling tin fog, increasing the amount of formic acid injection is beneficial for improving welding quality. Therefore, increasing the number of vacuum cycles, minimizing the vacuum degree, and enhancing the injection of formic acid could be a favorable direction for optimizing process parameters.

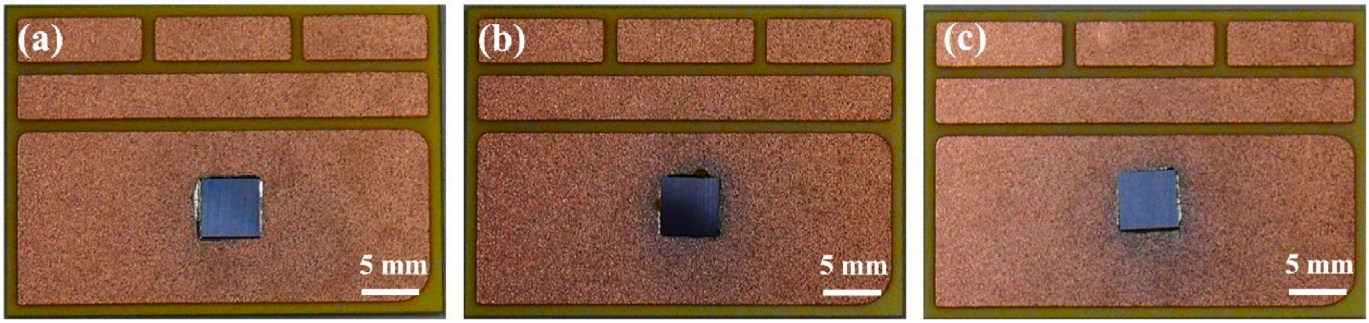

Fig. 18. Optical images of the prepared sample on DBC corresponding to the reflow profile (a) reflow profile h, (b) reflow profile i, (c) reflow profile j.

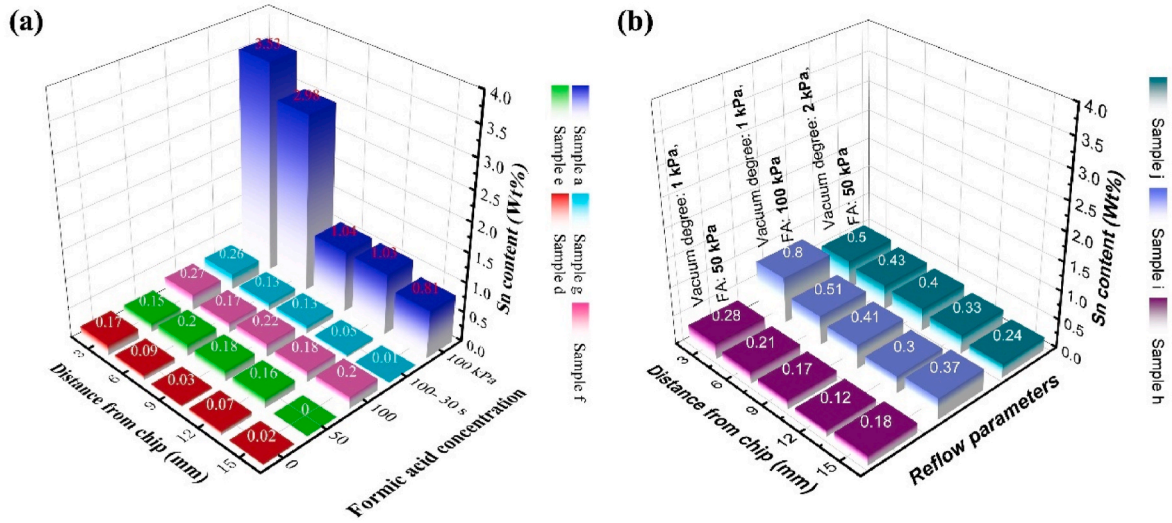

Fig. 19. Comparison of tin content distribution across different areas of the DBC substrate for prepared samples: (a) samples a, b, c, and d, (b) samples h, i, and j.

3.5. Al wire bonding and reliability verification for tin fog mitigation measures

In order to further validate the impact of tin fog, aluminum wire bonding was performed on the surfaces of samples e, f, and g, which were derived from the aforementioned optimized curves, and subsequently tested the shear strength before and after aging, followed by statistical analysis. The results are depicted in Fig. 20 below.

For sample e, obtained from reflow curve e, the average shear strength after surface bonding of Al wires was measured at 2087 g, with a standard deviation of 121.3 g. After aging in a muffle furnace at 300 °C for 4 h, the strength slightly increased to 2153.9 g, exhibiting a trend similar to that observed on pure copper surfaces, with a standard deviation of 159.6 g. Sample f, produced using the reflow curve with an increased formic acid pressure of 100 kPa, showed a shear strength of 2089.1 g before aging, with a standard deviation of 144.4 g, which increased to 2165.4 g post-aging, with a standard deviation of 154.1 g. Sample g, derived from reflow curve g with an extended 100 kPa formic acid duration of 30 s, demonstrated a shear strength of 2117.7 g before aging, with a standard deviation of 154.2 g, and 2177.9 g after aging, with a standard deviation of 167.6 g.

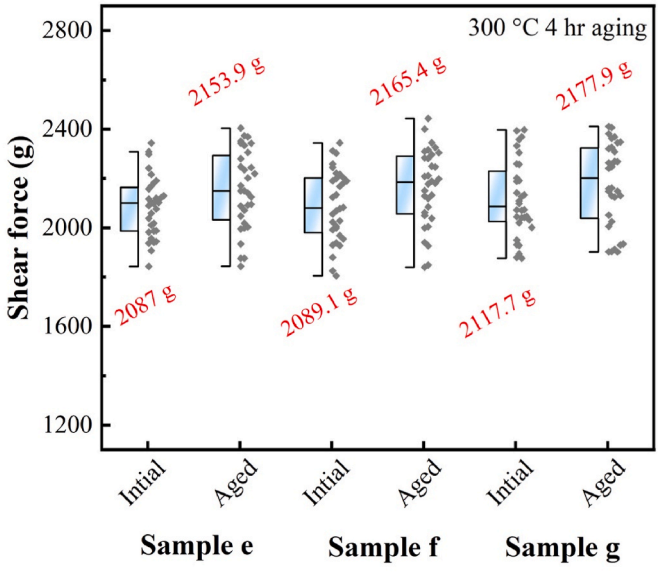

Fig. 20. The shear strength comparison among samples e, f, and g before and post-aging.

In all cases, the shear strength increased after aging, mirroring the upward trend observed on pure DBC surfaces. These results suggest that the curve designs aimed at controlling tin fog not only effectively manage the fog but also yield substrates whose aluminum wire bonding strength is comparable to pure DBC at the outset and maintain a similar trend post-aging.

Further works on IMC growth rate analysis, molecular dynamics simulation on crystallization influence, and different aging situations could further support the interaction between organic compounds from paste/preforms, various reflow settings, and the form of tin fog, thus providing a deeper understanding for the influence of tin fog on Al wire bond reliability.

4. Conclusion

In conclusion, our study has demonstrated the influence of tin fog on the reliability of aluminum wire bonding on DBC surfaces. Firstly, the influence of tin fog was analyzed. After 4 h of aging at 300 °C, the shear strength of wire bonds on pure copper surfaces rose by 4.5 %. Conversely, the shear strength of wire bonds on surfaces affected by tin fog dropped 22.6 %. Detailed SEM and EDS analyses pinpoint the formation of a porous structure at the bonding interface as a main factor.

Secondly, the mechanism of tin fog was examined. Through characterization techniques including SEM, EDS, Micro-IR, and XPS, the analysis revealed that specific organic compounds, notably long-chain molecules with carboxylic and amide groups, are instrumental in the development of tin fog. Such organic substances, along with tin derivatives, undergo decomposition and high-temperature oxidation during the reflow process on the substrate, ultimately depositing both tin and its oxides.

Thirdly, by optimizing the reflow parameters such as the vacuum application frequency, organic residues on the substrate are controlled, thereby effectively controlling tin fog formation, even under high formic acid conditions (up to 100 kPa for 32 s). This approach not only kept the incidence of tin fog negligible but also mirrored the strength of enhancements seen in pure DBC substrates, as reflected in reliability tests after aging at 300 °C for 4 h.

To sum up, this research provides insights into the effects of tin fog on substrates and the followed wire bonding reliability. Our findings suggest that strategic adjustments to reflow parameters play a critical role in enhancing the quality and sustainability of manufacturing processes in power electronics packaging.

CRediT authorship contribution statement

Liangzheng Ji: Conceptualization, Methodology, Investigation, Formal analysis, Writing – original draft. **Xinyue Wang:** Data curation, Formal analysis. **Wenting Liu:** Data curation, Formal analysis. **Xin Wang:** Data curation, Validation. **Wenwu Guo:** Data curation. **Guoqi Zhang:** Supervision. **Jing Zhang:** Formal analysis, Project administration, Supervision, Writing – review & editing. **Pan Liu:** Formal analysis, Project administration, Supervision, Writing – review & editing.

Declaration of generative AI and AI-assisted technologies in the writing process

During the preparation of this work, the authors used [ChatGPT 4o] in order to [polish the English language]. After using this tool/service, the authors reviewed and edited the content as needed and take full responsibility for the content of the publication.

Declaration of competing interest

The authors declare that they have no known competing financial interests or personal relationships that could have appeared to influence the work reported in this paper.

Acknowledgment

In this work, the authors would like to thank the Heraeus-Fudan cooperation project, under the support of Shanghai Science & Technology Communication (24500790700).

References

[1] Cheng S, Huang C-M, Pecht M. A review of lead-free solders for electronics applications. Microelectron Reliab 2017;75:77–95.
[2] Zhong S-j, Zhang L, Li M-l, Long W-m, Wang F-j. Development of lead-free interconnection materials in electronic industry during the past decades: structure and properties. Mater Des 2022:215.
[3] Mhd Noor EE, Mhd Nasir NF, Idris SRA. A review: lead free solder and its wettability properties. Solder Surf Mt Technol 2016;28(3):125–32.
[4] Efzan E, Marini A. A review of solder evolution in electronic application. Int J Eng Appl Sci 2012:1.
[5] Ramli MII, Salleh M, Abdullah M, Zaimi NSM, Sandu AV, Vizureanu P, Rylski A, Amli SFM. Formation and growth of intermetallic compounds in lead-free solder joints: a review. Materials 2022;15(4).
[6] Zhang H, Tan T, Yang M, Guo C, Yin L, Zhang L, Chai S. Formation mechanism for the interface between Cu and Sn formed by magnetic pulse welding. Mater Char 2024;208:113609.
[7] Zhang L, Hao G, Limeng Y, Hehe Z, Yao Z. Phase field simulation of interface evolution behavior of copper–tin micro-solder joints under thermal–mechanical–electrical coupling. J Adhes Sci Technol 2024;38(18):3506–24.
[8] Wakeel S, Haseeb ASMA, Afifi MA, Bingol S, Hoon KL. Constituents and performance of no-clean flux for electronic solder. Microelectron Reliab 2021;123.
[9] Conseil H, Verdingovas V, Jellesen MS, Ambat R. Decomposition of no-clean solder flux systems and their effects on the corrosion reliability of electronics. J Mater Sci Mater Electron 2016;27(1):23–32.
[10] Verdingovas V, Jellesen MS, Ambat R. Influence of sodium chloride and weak organic acids (flux residues) on electrochemical migration of tin on surface mount chip components. Corrosion engineering Science & Technology. 2013.
[11] Jacobson DM, Humpston G. Fluxless soldering. Int Mater Rev 2013;51(5):313–28.
[12] Hanss A, Elger G. Residual free solder process for fluxless solder pastes. Solder Surf Mt Technol 2018;30(2):118–28.
[13] He S, Shen Y-A, Xiong B, Huo F, Li J, Ge J, Pan Z, Li W, Hu C, Nishikawa H. Behavior of Sn-3.0Ag-0.5Cu solder/Cu fluxless soldering via Sn steaming under formic acid atmosphere. J Mater Res Technol 2022;21:2352–61.
[14] He S, Gao R, Shen Y-A, Li J, Nishikawa H. Wettability, interfacial reactions, and impact strength of Sn–3.0Ag–0.5Cu solder/ENIG substrate used for fluxless soldering under formic acid atmosphere. J Mater Sci 2019;55(7):3107–17.
[15] Conti F, Hanss A, Mokhtari O, Bhogaraju SK, Elger G. Formation of tin-based crystals from a SnAgCu alloy under formic acid vapor. New J Chem 2018;42(23):19232–6.
[16] Conti F, Hanss A, Fischer C, Elger G. Thermogravimetric investigation on the interaction of formic acid with solder joint materials. New J Chem 2016;40(12):10482–7.
[17] Bajwa A, Colosimo T, Grant T, Chylak B. Fluxless bonding of large area (≥ 900 mm2) dies-opportunities and challenges. In: 2021 IEEE 71st electronic components and technology Conference (ECTC); 2021. p. 457–61.
[18] Samson M, Oberson V, Paquin I, Fortin C, Raymond J-C, Bureau C, Barnes M, Zhao X, Wright D. Fluxless chip join process using formic acid atmosphere in a continuous mass reflow furnace. In: 2016 IEEE 66th Electronic Components and Technology Conference (ECTC); 2016. p. 574–9.
[19] He S, Gao R, Li J, Shen Y-A, Nishikawa H. In-situ observation of fluxless soldering of Sn-3.0Ag-0.5Cu/Cu under a formic acid atmosphere. Mater Chem Phys 2020;239.
[20] Mokhtari O, Conti F, Bhogaraju SK, Meier M, Schweigart H, Tetzlaff U, Elger G. Characterization of tin-oxides and tin-formate crystals obtained from SnAgCu solder alloy under formic acid vapor. New J Chem 2019;43(26):10227–31.
[21] Liu W, Wang X, Zhang J, Zhang G, Liu P. Al-clad Cu bond wires for power electronics packaging: microstructure evolution, mechanical performance, and molecular dynamics simulation of diffusion behaviors. Mater Today Commun 2024;41.
[22] Xu H, Liu C, Silberschmidt VV, Pramana SS, White TJ, Chen Z, Acoff VL. Behavior of aluminum oxide, intermetallics and voids in Cu–Al wire bonds. Acta Mater 2011;59(14):5661–73.
[23] Song F, Cen S, Wan C, Wang L. Nano-Au anchored in Organic base group-grafted silica aerogel: a durable and robust catalysts for green oxidative esterification of furfural. ChemCatChem 2022;14(18).
[24] Guo X, Qing Y, Wu Y, Wu Q. Molecular association of adsorbed water with lignocellulosic materials examined by micro-FTIR spectroscopy. Int J Biol Macromol 2016;83:117–25.
[25] Mo Z, Liu H, Hu R, Gou H, Li Z, Guo R. Amino-functionalized graphene/chitosan composite as an enhanced sensing platform for highly selective detection of Cu2+. Ionics 2017;24(5):1505–13.
[26] Chen Z, Wang J, Chao D, Baikie T, Bai L, Chen S, Zhao Y, Sum TC, Lin J, Shen Z. Hierarchical porous LiNi1/3Co1/3Mn1/3O2 nano-/micro spherical cathode material: minimized cation mixing and improved Li(+) mobility for enhanced electrochemical performance. Sci Rep 2016;6:25771.
[27] Graf N, Yegen E, Gross T, Lippitz A, Weigel W, Krakert S, Terfort A, Unger WES. XPS and NEXAFS studies of aliphatic and aromatic amine species on functionalized surfaces. Surf Sci 2009;603(18):2849–60.
[28] Ji L, Zhang J, Zhang G, Liu P. A polyamide-facilitated soldering approach for Mini LED precise alignment leveraging 3D interfacial networks. J Sci: Advanced Materials and Devices 2024;9(4).
[29] Richstein R, Eisen C, Ge L, Chalermnon M, Mayer F, Keppler BK, Chin JM, Reithofer MR. NHC stabilized copper nanoparticles via reduction of a copper NHC complex. Chem Commun 2023;59(64):9738–41.
[30] Sohn Y, Pradhan D, Zhao L, Leung KT. Anomalous oxidation resistance of "core-only" copper nanoparticles electrochemically grown on gold nanoislands prefunctionalized by 1,4-phenylene diisocyanide. Electrochem Solid State Lett 2012;15(4).
[31] Ozawa N, Okubo T, Shibata M. Relationship between the reduction behavior of Copper and Tin Oxide Films by Formic acid and Solder. Wettability 2020;71(4):293–7.